Supplementary Materials

Integrated PredRNN++ and phase-field for microstructure prediction and simulation acceleration

Junpeng Song[1,2,#], Shenglong Wang[1,2,#], Zan Zhang[1,2], Kunning Niu[1,2], Ye Shan[1,2], Yongsheng Li[1,2]

[1]School of Materials Science and Engineering, Nanjing University of Science and Technology, Nanjing 210094, Jiangsu, China.
[2]MIIT Key Laboratory of Advanced Metallic and Intermetallic Materials Technology, Nanjing 210094, Jiangsu, China.

[#]Authors contributed equally.

Correspondence to: Prof. Yongsheng Li, School of Materials Science and Engineering, Nanjing University of Science and Technology, Nanjing 210094, Jiangsu, China. E-mail: ysli@njust.edu.cn

Phase-field model

The Cahn-Hilliard and Ginzburg-Landau equations are used in the PF simulation for precipitates evolution in superalloys, these control the evolution of composition field $c_i(\mathbf{r},t)$ and order parameter field $\eta_p(\mathbf{r},t)$[1].

$$\frac{\partial c_i(\mathbf{r},t)}{\partial t} = V_m^2 \nabla \left[M_i \nabla \left(\frac{\delta F}{\delta c_i(\mathbf{r},t)} \right) \right] + \xi_c(\mathbf{r},t) \tag{1}$$

$$\frac{\partial \eta_p(\mathbf{r},t)}{\partial t} = -L \left(\frac{\delta F}{\delta \eta_p(\mathbf{r},t)} \right) + \xi_\eta(\mathbf{r},t) \tag{2}$$

where $\xi_c(\mathbf{r},t)$ and $\xi_\eta(\mathbf{r},t)$ are noise items in composition and order parameters, V_m is the molar volume of the alloy, F is the total energy, M_i are the chemical mobilities of different elements, and L is the interface mobility.

$$M_i = \frac{D_i}{\left(V_m \frac{\partial^2 f^\gamma}{\delta c_i^2} \right)} \tag{3}$$

$$D_i = D_0 exp\left(-\frac{\Delta U}{kT} \right) \tag{4}$$

D_0 is the diffusion constant, i represents the elements in each superalloy system[2, 3]. The Gibbs free energy consists of chemical free energy f_{ch}, gradient interface energy f_{int}, and elastic strain energy f_{el},

$$F = \int_V [f_{\mathrm{ch}} + f_{\mathrm{int}} + f_{\mathrm{el}}] dV \tag{5}$$

where f_{ch} is the chemical free energy density, f_{int} is the interfacial energy density, and f_{el} is the elastic strain energy density[4, 5].

The chemical free energy density coupling with the KKS model of different superalloy systems can be written as[5],

$$f_{\mathrm{ch}}\left(c_i, \{\eta_p\}, T\right) = V_m^{-1} \left[1 - \sum_{p=1}^{3} h\left(\eta_p\right) \right] f^\gamma\left(c_i^\gamma, T\right)$$

$$+ V_m^{-1} \sum_{p=1}^{3} h\left(\eta_p\right) f^{\gamma'}\left(c_i^{\gamma'}, T\right) + \varpi g\left(\{\eta_p\}\right) \tag{6}$$

where $f^\gamma(c_i^\gamma, T)$ and $f^{\gamma'}\left(c_i^{\gamma'}, T\right)$ are the molar Gibbs energy density of γ and γ′ phase, $f^\gamma(c_i^\gamma, T)$ and $f^{\gamma'}\left(c_i^{\gamma'}, T\right)$ can be approximated by a parabola, and expressed in the form of the second-order expansion of Taylor series with equilibrium composition, i

represents the elements in each superalloy system, ϖ is a parameter in depicting the height of the double-well function, $h(\eta_p)$ is the interpolation function coupled with the matrix and precipitate phases, $g(\eta_p)$ is Landau double-well function used to eliminate the coexistence of different domains of γ' phase in the same position[6]. These functions are as follows,

$$h(\eta_p) = \eta_p^3(6\eta_p^2 - 15\eta_p + 10) \tag{7}$$

$$g(\eta_p) = \sum_{p=1}^{3} \eta_p^2 (1 - \eta_p^2) + \theta \sum_{p \neq q} \eta_p^2 \eta_q^2 \quad q = 1, 2, 3 \tag{8}$$

where θ is assumed to satisfy the lowest energy principle[7].

The interfacial energy can be calculated by the interface gradient,

$$f_{\mathrm{int}} = \int_V \left[\frac{1}{2} \sum_i k_i (\nabla c_i)^2 + \frac{1}{2} k_\eta \sum\nolimits_{p=1}^{3} \left(\nabla \eta_p \right)^2 \right] dV \tag{9}$$

where k_i and k_η are the interfacial energy coefficients of composition and order parameters, and we assume that the interfacial energy coefficients of different components are equal[8, 9].

The elastic strain energy f_{el} is calculated by the microscopic elastic theory[10],

$$f_{\mathrm{el}} = \int_V \left[\frac{1}{2} C_{ijkl} \varepsilon_{ij}^{\mathrm{el}}(\mathbf{r}) \varepsilon_{kl}^{\mathrm{el}}(\mathbf{r}) \right] dV \tag{10}$$

where $\varepsilon_{ij}^{\mathrm{el}}(\mathbf{r})$ is elastic strain, $\varepsilon_{ij}^{\mathrm{el}}(\mathbf{r}) = \bar{\varepsilon}_{ij}(\mathbf{r}) + \delta\varepsilon_{ij}(\mathbf{r}) - \varepsilon_{ij}^{0}(\mathbf{r})$. $\bar{\varepsilon}_{ij}(\mathbf{r})$ and $\delta\varepsilon_{ij}(\mathbf{r})$ are the homogeneous strain and heterogeneous strain, respectively. $\varepsilon_{ij}^{0}(\mathbf{r})$ is eigenstrain. The C_{ijkl} is elastic modulus, $C_{ijkl} = \bar{C}_{ijkl} + \Delta C_{ijkl} \Delta c(\mathbf{r})$. The ΔC_{ijkl} is the difference in elastic modulus between the precipitated phase and matrix, $\bar{C}_{ijkl}$ is the average elastic modulus, $C_{ijkl}^{\gamma'}$ and C_{ijkl}^{γ} are the elastic modulus of the precipitated phase and the matrix phase, respectively.

$$\varepsilon_{ij}^{0}(\mathbf{r}) = \delta \sum_{p=1}^{3} h(\eta_p)\, \delta_{ij} \tag{11}$$

where δ_{ij} is the Kronecker-delta function, δ is the lattice mismatch between γ/γ' phases[11].

The dimensionless parameters are given as, $t^* = L\Delta f t$, $r^* = \frac{r}{l}$, $k_i^* = \frac{k_i}{\Delta f l^2}$, $k_\eta^* = \frac{k_\eta}{\Delta f l^2}$, $\nabla^* = \frac{\partial}{\partial (r/l)}$, $M_i^* = \frac{V_m M_i}{L l^2}$, $f_{\mathrm{ch}}^* = \frac{f_{\mathrm{ch}}}{\Delta f}$, $f_{\mathrm{el}}^* = \frac{f_{\mathrm{el}}}{\Delta f}$. The semi-implicit Fourier spectral algorithm is used to solve these equations in a cell with grids 256×256[12]. The phase-field model parameters are listed in Supplementary Table 1.

Among the variables in this study, the change of k_η will affect the magnitude of the interface energy f_{int} and the change of δ will affect the magnitude of the elastic strain energy f_{el}.

Supplementary Table 1. Phase-field model parameters for different composition systems.

System	**Ni-Al superalloy**[13]	**Co-10Al-10W(at.%)**[2]	**Ni-10Al-8.5Cr-2Ta (at.%)**[1]
$\xi_c(\mathbf{r},t)$	0.0006	0.0003	0.0001
$\xi_\eta(\mathbf{r},t)$	0.0012	0.0003	0.0001
$D_0/\mathrm{m}^2\cdot\mathrm{s}^{-1}$	1.46×10^{-2}	1.45×10^{-4}	1.45×10^{-4}
T/K	873	1173	1073
$\Delta U/\mathrm{eV}$	2.8	2.8	2.8
$\Delta f/\mathrm{J}\cdot\mathrm{m}^{-3}$	3.3×10^{7}	6×10^{6}	3×10^{7}
l/m	1.5×10^{-9}	1.5×10^{-9}	2×10^{-9}
$\Delta t^*/s$	3×10^{-2}	2×10^{-2}	1×10^{-2}
$C_{11}^{\gamma}/\mathrm{GPa}$	214	230	262
$C_{12}^{\gamma}/\mathrm{GPa}$	150	170	158
$C_{44}^{\gamma}/\mathrm{GPa}$	100	90	82.8
$C_{11}^{\gamma'}/\mathrm{GPa}$	212	253	262
$C_{12}^{\gamma'}/\mathrm{GPa}$	149	247	158
$C_{44}^{\gamma'}/\mathrm{GPa}$	106	117	82.8
Storage interval/Round	10000	10000	10000
Total steps/Round	500000	1200000	1000000
Total time/s	15000	24000	10000

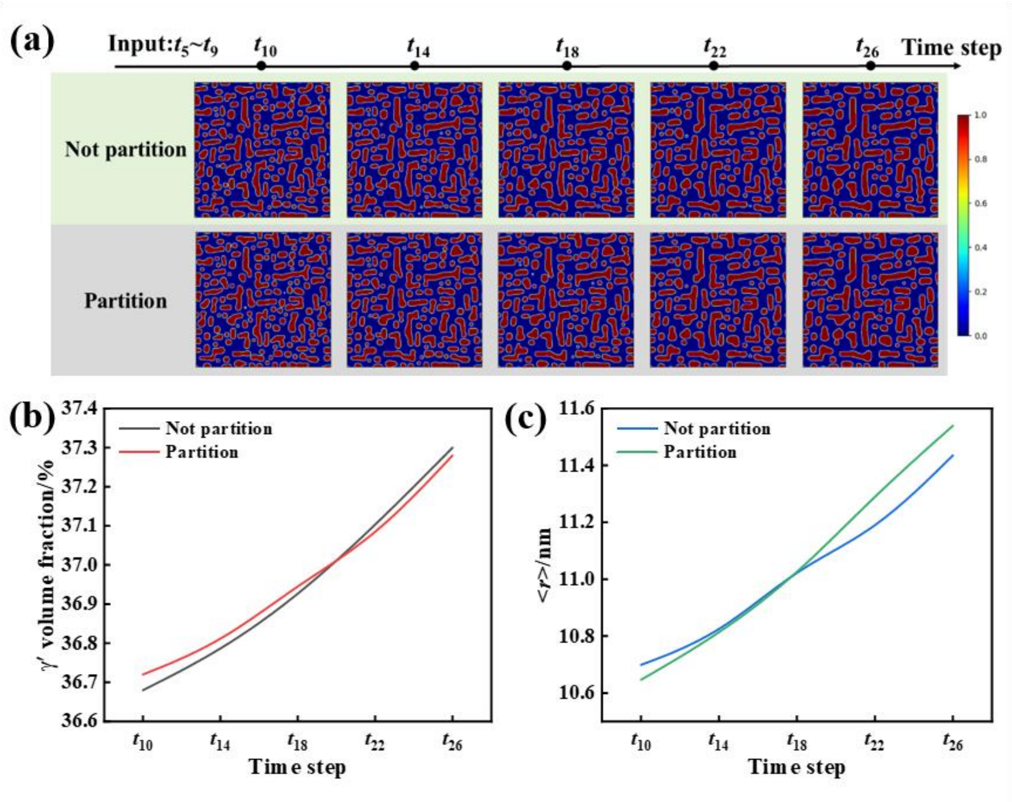

Supplementary Figure 1. Comparison of microstructures with or without partition, (a) microstructure, (b) γ′ volume fraction, (c) average radius.

Supplementary Table 2. Ni-Al superalloy dataset

System	**Ni-Al superalloy**
Shape definition	Mixed
Deep learning training time steps	[t_5, t_{50}]
Variable	Composition (c_{Al}) and interfacial energy coefficient(k_η) c_{Al}=0.154–0.159, interval: 0.001 k_η=0.05—0.10, interval: 0.01
Training set	c_{Al}=0.154–0.158, (4320, 5, 2, 128, 128)
Testing set	c_{Al}=0.159, (864, 5, 2, 128, 128)

Supplementary Table 3. Co-10Al-10W(at.%) superalloy dataset

System	**Co-10Al-10W(at.%)**
Shape definition	Cubic
Deep learning training time steps	[t_{15}, t_{119}]
Variable	Lattice mismatch (δ) δ=0.002–0.006, interval: 0.001
Training set	δ=0.002–0.005, (1568, 8, 5, 128, 128)
Testing set	δ=0.006, (392, 8, 5, 128, 128)

Supplementary Table 4. Ni-10Al-8.5Cr-2Ta (at.%) superalloy dataset

System	**Ni-10Al-8.5Cr-2Ta (at.%)**
Shape definition	Circular
Deep learning training time steps	[t_{15}, t_{100}]
Variable	Interfacial energy coefficient (k_η) and Lattice mismatch(δ) k_η=6.32–8.82, interval: 0.5 δ=0.0029–0.0049, interval: 0.0005
Training set	k_η=6.32–8.32, (8400, 5, 6, 128, 128)
Testing set	k_η=8.82, (1200, 5, 6, 128, 128)

Comparison of deep learning models

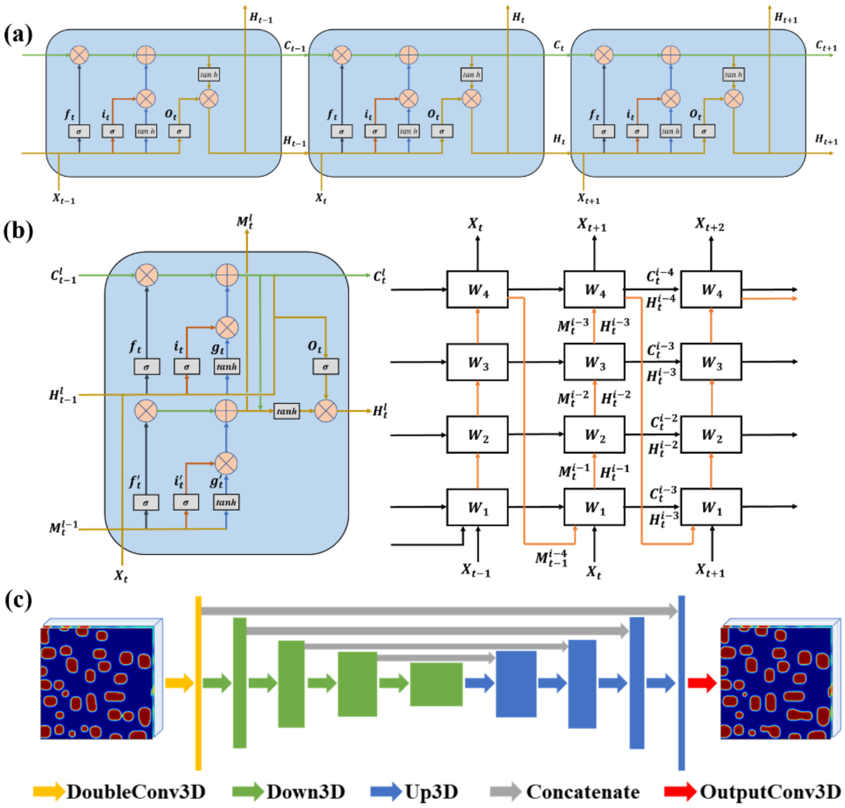

Supplementary Figure 2. The schematic diagrams of other deep learning model frameworks, (a) ConvLSTM, (b) PredRNN, (c) CNN.

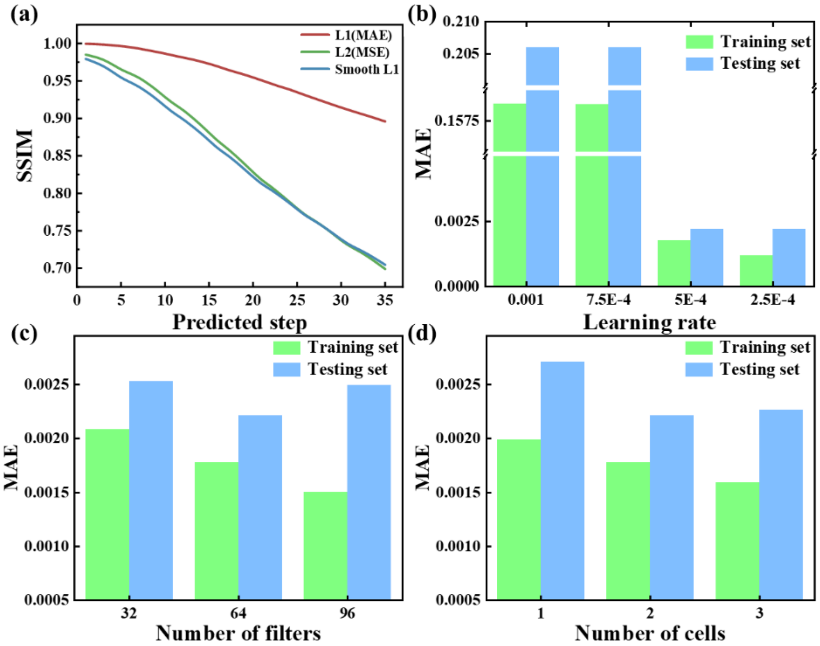

Supplementary Figure 3. Hyperparameter optimization for the PredRNN++ model, (a) loss functions, (b) learning rate, (c) number of filters, (d) number of cells.

Model performance evaluation of PredRNN++ model

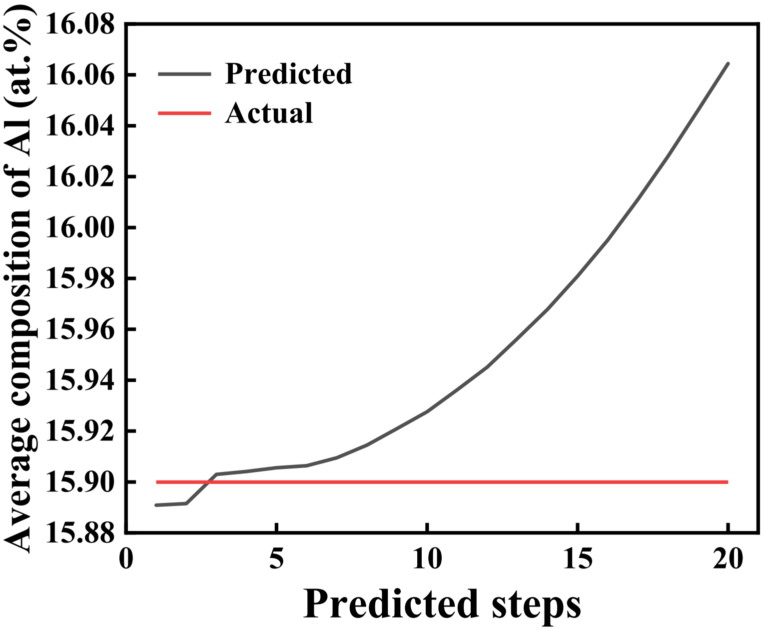

Supplementary Figure 4. Evolution of the average composition of Al (at.%) of the PredRNN++ model as a function of predicted steps.

Accelerated phase-field simulation

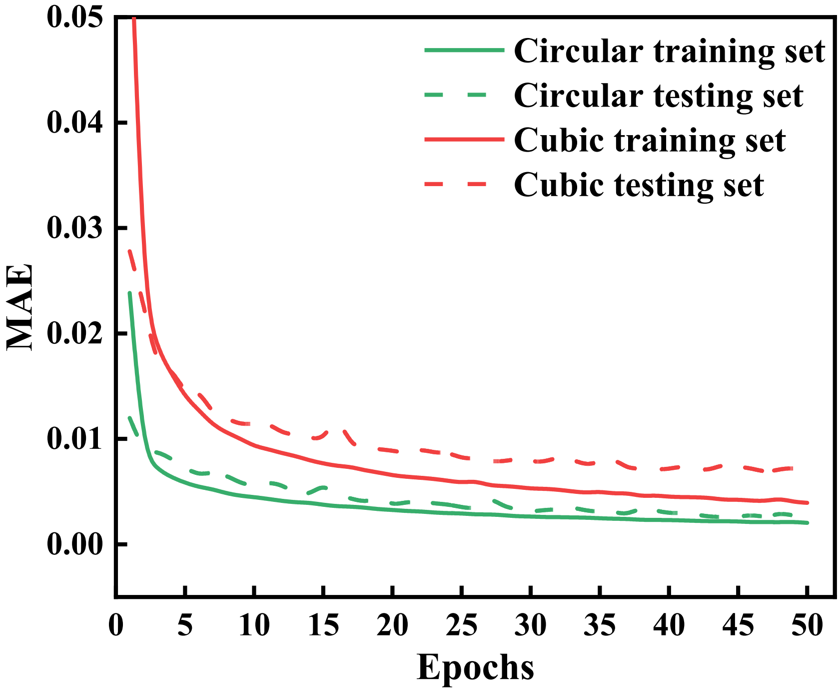

Supplementary Figure 5. The MAE loss curves for different shapes.

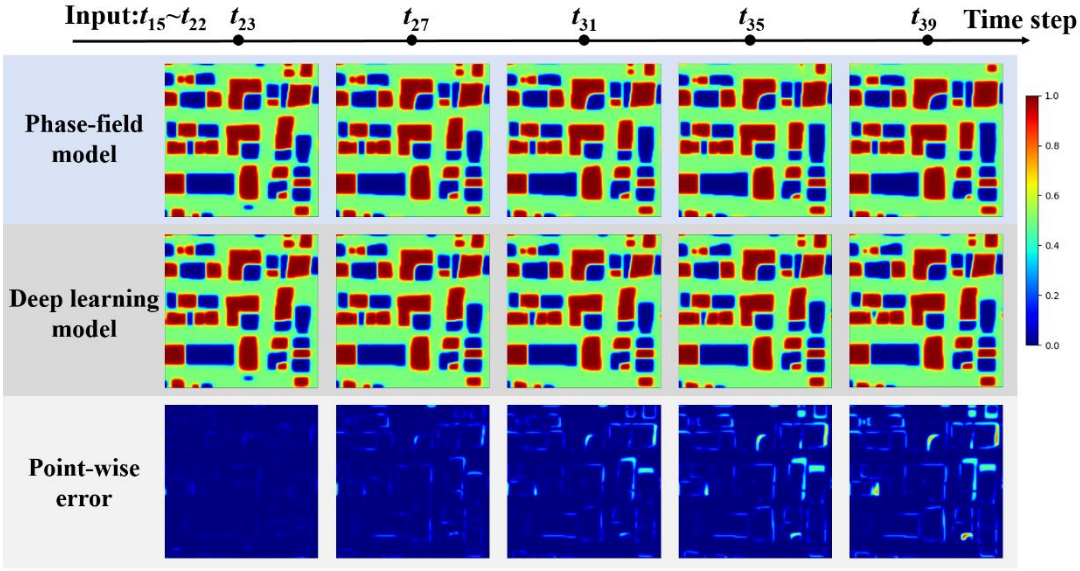

Supplementary Figure 6. Predicted results of PredRNN++ model by using the cubic precipitates of

PF input morphology of step t_{15}–t_{22} with Co-10Al-10W (at.%) superalloy.

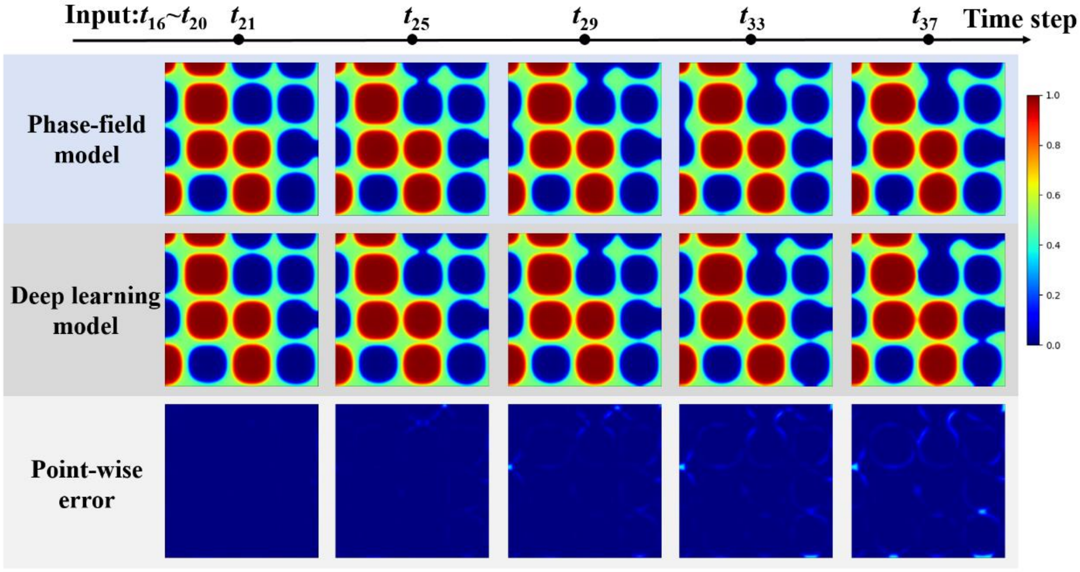

Supplementary Figure 7. Predicted results of PredRNN++ model by using the circular precipitates

of PF input morphology of step t_{16}–t_{20} with Ni-10Al-8.5Cr-2Ta (at.%) superalloy.

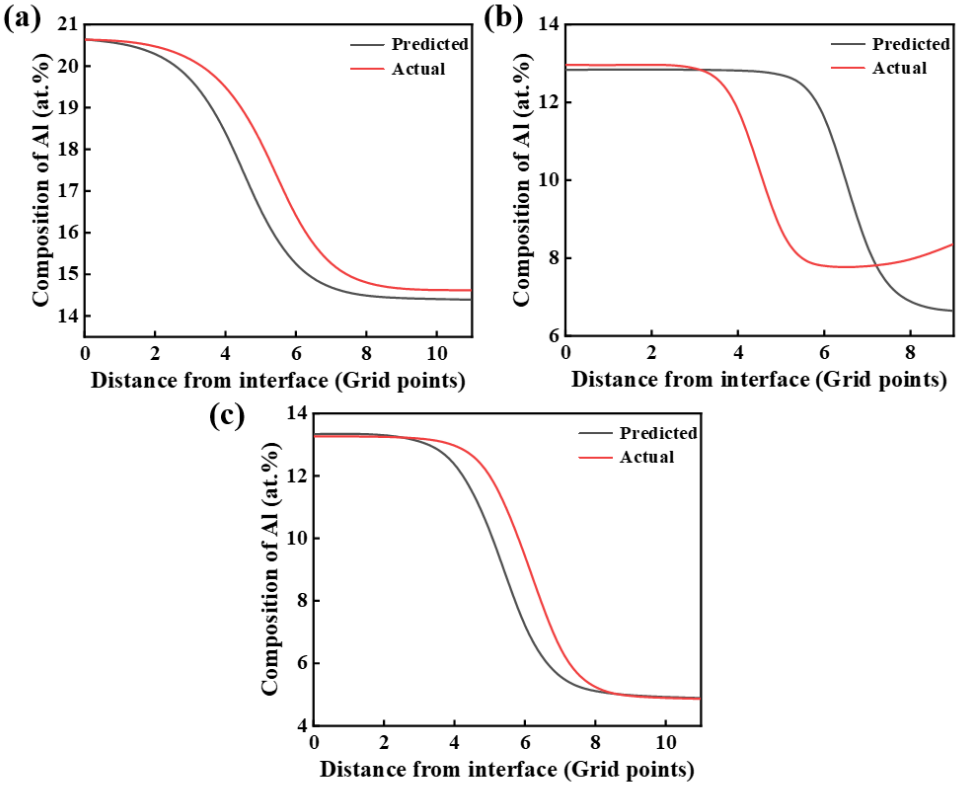

Supplementary Figure 8. Composition of Al in the PredRNN++ model at the predicted step of 20, (a)Ni-15.9Al (at.%) of Figure 8, (b) Co-10Al-10W (at.%) of Supplementary Figure 5, (c) Ni-10Al-8.5Cr-2Ta (at.%) of Supplementary Figure 6.

REFERENCES

1. Wang S, Song J, Shan Y, et al. Lattice strain and composition regulated morphology kinetics with antiphase boundary in Co-based superalloy. Materials & Design. 2025, 257: 114522. https://doi.org/10.1016/j.matdes.2025.114522
2. Yang S, Zhang Z, Zhuo J, et al. Phase-field simulation of precipitation kinetics and creep properties of Ni-Al-Cr/Ta superalloys. Science China Technological Sciences. 2024, 67: 1139–1150. https://doi.org/10.1007/s11431-023-2424-9
3. Gaubert A, Bouar Y L, Finel A. Coupling phase field and viscoplasticity to study rafting in Ni-based superalloys. Philosophical Magazine. 2010, 90: 1–4. https://doi.org/10.1080/14786430902877802
4. Ali M A, Shchyglo O, Stricker M, et al. Coherency loss marking the onset of degradation in high temperature creep of superalloys: Phase-field simulation

coupled to strain gradient crystal plasticity. Computational Materials Science. 2023, 220: 112069. https://doi.org/10.1016/j.commatsci.2023.112069

5. Ji Y, Lou Y, Qu M, et al. Predicting coherency loss of γ″ precipitates in IN718 superalloy. Metallurgical and Materials Transactions A. 2016, 47: 3235–3247. https://doi.org/10.1007/s11661-016-3480-0
6. Zhou N, Shen C, Mills M, et al. Large-scale three-dimensional phase field simulation of γ′-rafting and creep deformation. Philosophical Magazine. 2010; 90: 405–436. https://doi.org/10.1080/14786430903081990
7. Ju, Y, Long H, Qin Q, et al. Creep property and rafting kinetics of Co-based monocrystal superalloys with antiphase boundaries of γ′ phase. Materials Science and Engineering: A. 2023; 880: 145283. https://doi.org/10.1016/j.msea.2023.145283.
8. Meher S, Nag S, Tiley J, et al. Coarsening kinetics of γ′ precipitates in cobalt-base alloys. Acta Materialia. 2013, 61: 4266–4276. https://doi.org/10.1016/j.actamat.2013.03.052
9. Shi S, Li Y, Yan Z, et al. Crystal plasticity phase-field simulation of slip system anisotropy during creep of Co-Al-V monocrystal alloy under multidirectional strain. International Journal of Mechanical Sciences. 2022, 227: 107436. https://doi.org/10.1016/j.ijmecsci.2022.107436
10. Shi S, Li Y, Yan Z, et al. Crystal plasticity phase-field simulation of slip system anisotropy during creep of Co-Al-V monocrystal alloy under multidirectional strain. International Journal of Mechanical Sciences. 2022, 227: 107436. https://doi.org/10.1016/j.ijmecsci.2022.107436
11. Wu R, Zaiser M. Cyclic-loading microstructure-property relations from a mesoscale perspective: An example of single crystal Nickel-based superalloys. Journal of Alloys and Compounds. 2019, 770: 964–971. https://doi.org/10.1016/j.jallcom.2018.08.168
12. Shan Y, Zhuo J, Song J, et al. Precipitation kinetics and creep properties of multicomponent Ni-based superalloys. Journal of Materials Science. 2024, 59: 20715–20734. https://doi.org/10.1007/s10853-024-10275-6

13. Zhou X R, Li Y S, Yan Z W, et al. Kinetics of Overlapping Precipitation and Particle Size Distribution of Ni_3Al Phase. Physics of Metals and Metallography, 2019, 120(4): 345–352. https://doi.org/10.1134/S0031918X19040045